Quantitative Evaluation of 2 Scatter-Correction Techniques for ^{18}F-FDG Brain PET/MRI in Regard to MR-Based Attenuation Correction

Jarmo Teuho[1,2], Virva Saunavaara[2,3], Tuula Tolvanen[2,3], Terhi Tuokkola[2], Antti Karlsson[3,4], Jouni Tuisku[2], and Mika Teräs[3,5]

[1]Turku PET Centre, University of Turku, Turku, Finland; [2]Turku PET Centre, Turku University Hospital, Turku, Finland; [3]Department of Medical Physics, Turku University Hospital, Turku, Finland; [4]Turku Centre for Quantum Physics, Department of Physics and Astronomy, University of Turku, Turku, Finland; and [5]Institute of Biomedicine, University of Turku, Turku, Finland

In PET, corrections for photon scatter and attenuation are essential for visual and quantitative consistency. MR attenuation correction (MRAC) is generally conducted by image segmentation and assignment of discrete attenuation coefficients, which offer limited accuracy compared with CT attenuation correction. Potential inaccuracies in MRAC may affect scatter correction, because the attenuation image (μ-map) is used in single scatter simulation (SSS) to calculate the scatter estimate. We assessed the impact of MRAC to scatter correction using 2 scatter-correction techniques and 3 μ-maps for MRAC. **Methods:** The tail-fitted SSS (TF-SSS) and a Monte Carlo–based single scatter simulation (MC-SSS) algorithm implementations on the Philips Ingenuity TF PET/MR were used with 1 CT-based and 2 MR-based μ-maps. Data from 7 subjects were used in the clinical evaluation, and a phantom study using an anatomic brain phantom was conducted. Scatter-correction sinograms were evaluated for each scatter correction method and μ-map. Absolute image quantification was investigated with the phantom data. Quantitative assessment of PET images was performed by volume-of-interest and ratio image analysis. **Results:** MRAC did not result in large differences in scatter algorithm performance, especially with TF-SSS. Scatter sinograms and scatter fractions did not reveal large differences regardless of the μ-map used. TF-SSS showed slightly higher absolute quantification. The differences in volume-of-interest analysis between TF-SSS and MC-SSS were 3% at maximum in the phantom and 4% in the patient study. Both algorithms showed excellent correlation with each other with no visual differences between PET images. MC-SSS showed a slight dependency on the μ-map used, with a difference of 2% on average and 4% at maximum when a μ-map without bone was used. **Conclusion:** The effect of different MR-based μ-maps on the performance of scatter correction was minimal in non–time-of-flight ^{18}F-FDG PET/MR brain imaging. The SSS algorithm was not affected significantly by MRAC. The performance of the MC-SSS algorithm is comparable but not superior to TF-SSS, warranting further investigations of algorithm optimization and performance with different radiotracers and time-of-flight imaging.

In brain PET/MRI, accurate scatter and attenuation correction are essential for image quality and quantitative accuracy of reconstructed PET images. Scatter and attenuation correction are closely connected because emission and attenuation images are used to estimate the amount of scattered photons in single scatter simulation (SSS), which relies on the accuracy of the estimated emission images and the μ-map (1). Therefore, the accuracy of the μ-map will also contribute to the performance of SSS. However, only limited investigations have been performed about the effect of the accuracy of the μ-map on the performance of SSS in PET/MRI (2).

In PET/MRI, the accuracy of the μ-map is limited in MR attenuation correction (MRAC) compared with CT attenuation correction (CTAC). Because linear attenuation coefficients cannot be measured from MR images as in CT, photon attenuation needs to be estimated by other means, commonly by image segmentation (3). The resulting MR-based μ-map will inherently be an approximation of the true attenuation. Because this μ-map is used in scatter correction, inconsistencies in PET image quantification may result. Therefore, it is critical to investigate the effect of MRAC on the performance of current scatter-correction techniques for brain PET/MRI with different μ-maps (2).

In the Philips Ingenuity TF PET/MR scanner, scatter correction can be applied by 2 techniques: the tail-fitted SSS (TF-SSS) and the Monte Carlo–based single scatter simulation (MC-SSS). The main difference between the algorithms is how the scaling factors are derived for matching the scatter sinogram to measured emission data. The scaling is performed either by tail fitting (TF-SSS) or by low-count Monte Carlo (MC) simulation (MC-SSS) (4). A short description of vendor-specific implementations of TF-SSS and MC-SSS algorithms is given below.

The SSS algorithm models the contribution of single scatter events where an annihilation photon has been scattered only once (1,2,4–8). It is assumed that total scatter including single and multiple scatter can be derived from a scaled distribution of single scatter (1,2,4–8). The scatter estimate needs to be scaled to match
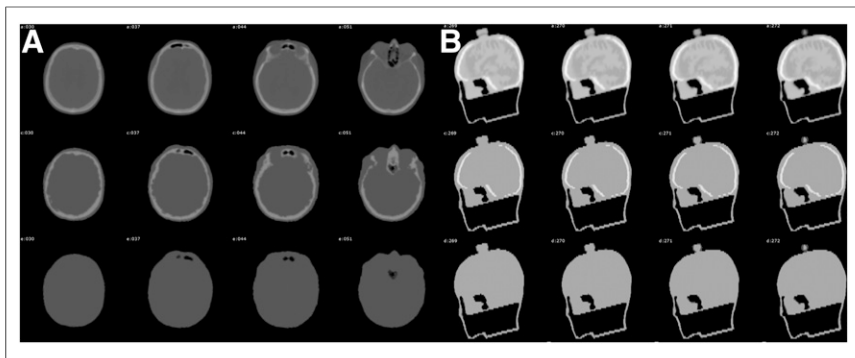
FIGURE 1. Visualization of CT- and MR-based μ-maps of clinical subject (A) and phantom (B). CT-based μ-maps are presented in first row, and MRAC$_{3class}$ and MRAC$_{2class}$ μ-maps are presented in second and third rows. Window level between μ-maps is set same.

the emission data, where scaling is implemented as a linear transformation (*1,2,4–8*). The scaling parameters can be derived by fitting SSS data with a least-mean-squares technique to the scatter tails of the emission data (tail fitting) (*1,2,4–8*). The tail part of the scatter sinogram is determined by deriving a mask from the attenuation-correction sinogram. The tails correspond to the emission lines of response that do not pass through the object, representing pure scatter (*1,2,4–8*). After tail fitting, the scaled scatter distribution is subtracted from the normalized emission data (*1,2,4–8*). This vendor-specific version of the TF-SSS is considered an accurate and computationally efficient technique for scatter correction.

MC-SSS is a novel approach, using a combination of SSS and low-count MC simulation to derive the scaling parameters instead of tail fitting (*4*). The scatter contribution shape is realized by SSS and the scaling factor is determined by an MC simulation to match the SSS sinogram to the emission data (*4*). Because the scaling factors are derived by an MC simulation, the accuracy of the scaling parameters is not dependent on the quality of tail fitting. This can be considered to be an advantage of the MC-SSS algorithm over TF-SSS. However, initial evaluations of MC-SSS have been performed only for whole-body imaging, with no implications or thorough regional analysis performed for the brain in PET/MRI (*4,9*), where the effect of MRAC is more pronounced, especially when bone is ignored. Therefore, evaluation of the MC-SSS algorithm for brain PET/MRI is warranted.

Our aim was to evaluate the effect of MRAC on 2 scatter-correction techniques in brain PET/MR with 3 methods for MRAC.

We hypothesized that the scatter-correction techniques should be largely unaffected by the inaccuracies of MRAC in static ^{18}F-FDG brain imaging and would not expect large differences in quantitative performance in clinical scan conditions. Although MRAC in PET/MRI has been studied extensively (*3*), there are no known clinical reports on the performance of scatter algorithms with different methods for MRAC.

MATERIALS AND METHODS

Patient Population

The study protocol was approved by an institutional review board (Ethics Committee) and the radiation protection authorities and was performed according to the latest version of the Declaration of Helsinki. All subjects signed a written informed consent form. Subjects who had undergone PET/MR and PET/CT examination during the same day with a single-injection and dual-imaging protocol were included in the patient material. All patients had been referred to our institute for a clinical routine PET/CT ^{18}F-FDG PET brain examination with an additional PET/MR examination. The CTAC data from the PET/CT examination was used in the evaluation as a reference method for PET/MR attenuation correction. The clinical data included 7 subjects (3 men and 4 women) with a median and range of age and weight of 47 y (26–74 y) and 77 kg (47–80 kg), respectively. A patient with a metal implant was included in the study.

PET/MR and PET/CT Imaging Protocol

All subjects had undergone a PET/MR (Ingenuity TF PET/MR; Philips Healthcare) and a PET/CT (Discovery 690 PET/CT; GE Healthcare) examination performed in a randomized fashion. The physical performance of both systems has been described previously (*10,11*). Patients were administered ^{18}F-FDG depending on their body weight. The median dose and range were 274 MBq (199–299 MBq), and the mean (±SD) of the first PET scan start times was 80 ± 20 min after injection. The PET/CT and PET/MR examinations were conducted using the standard protocol for neuroimaging at our institute.

The PET/MRI consisted of T1-weighted 3-dimensional fast field echo for clinical MRAC followed by a PET examination. An 8-channel head coil was used for MR imaging. The parameters for
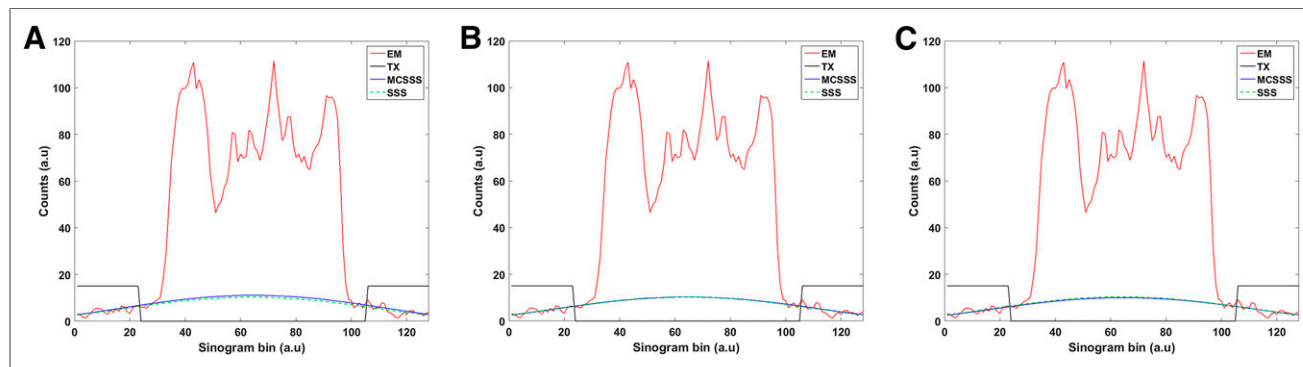

FIGURE 2. Measured sinogram profiles from randoms-corrected emission sinogram (EM), transmission sinogram mask (TX), and scatter-correction sinograms from TF-SSS and MC-SSS for phantom. Shown is CTAC- (A), MRAC$_{3class}$- (B), and MRAC$_{2class}$- (C) reconstructed PET, respectively.
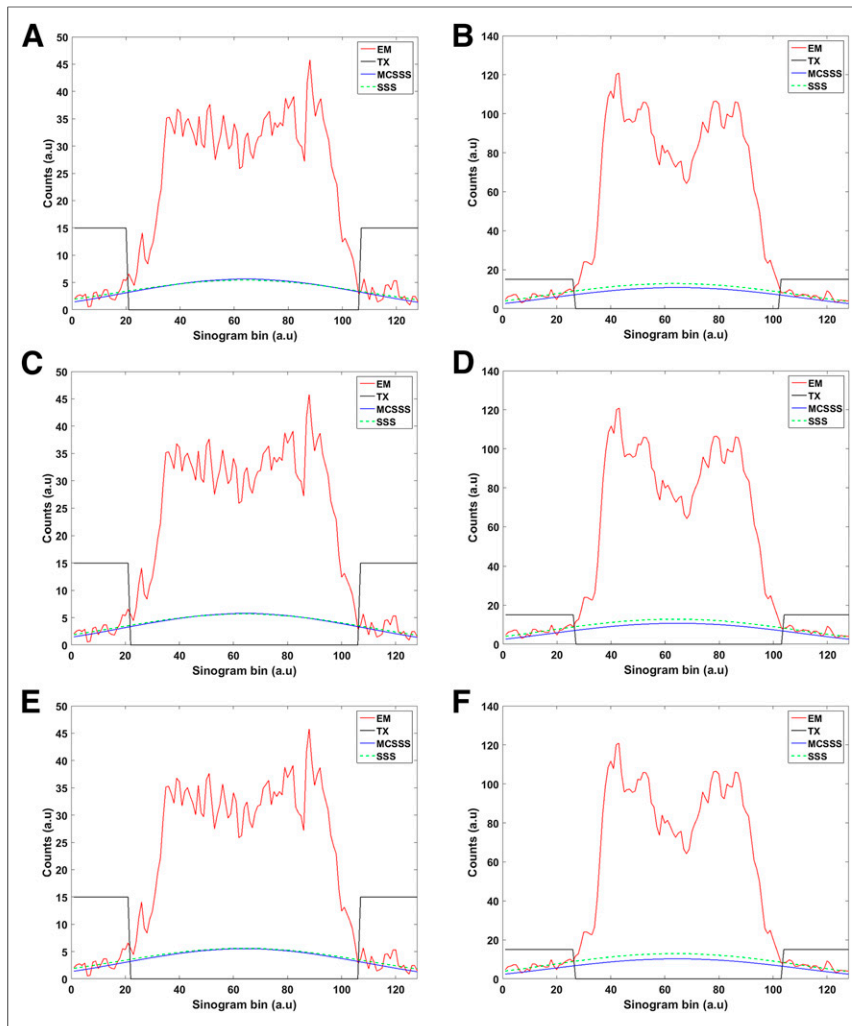
FIGURE 3. Measured sinogram profiles from randoms-corrected emission sinogram (EM), transmission sinogram mask (TX), and scatter sinograms from TF-SSS and MC-SSS for 2 subjects (subjects 4 and 1). Best (left) and worst case showing poorer fit for MC-SSS (right) are presented. Shown is CTAC- (A and B), MRAC$_{3class}$- (C and D), and MRAC$_{2class}$- (E and F) reconstructed PET.

MRAC were an echo time of 2.16 ms, repetition time of 4.18 ms, flip angle of 10°, field of view of 320 mm, and acquisition time of 84 s. The PET image was acquired with a transaxial field of view of 256 mm, over 1 bed position covering the entire head region, with a duration of 15 min.

At the PET/CT, a low-dose CTAC with tube voltage of 120 kV using automatic dose modulation with 10 mAs was acquired and was

used as the reference method for PET/MR attenuation correction in this study.

3-Dimensional Brain Phantom Imaging Protocol

A phantom scan was obtained to complement the patient data. A standard National Electrical Manufacturers Association (NEMA) scatter phantom and a 3-dimensional printed anatomic brain phantom (Iida phantom) were used (12). The NEMA scatter phantom was placed approximately 8 cm apart from the brain phantom to simulate scatter originating from the patient body in a clinical brain scan. Phantoms were fixed by straps to prevent motion in the MR and PET scans. Foam pads were used to support the phantom head on the bed.

The phantom measurements were done on the same PET/MR and PET/CT systems as the patient scans, using a similar scan protocol for PET, MR, and CT. All PET scans were obtained in list-mode, with a scan duration of 15 min without a head coil on the PET/MR. Afterward, the phantom was transferred to the PET/CT, where a standard low-dose CTAC using a tube voltage of 120 kV was collected for reference method for PET/MR attenuation correction.

The brain phantom gray matter compartment was filled with 40 MBq of radioactivity in 750 mL of water whereas the NEMA scatter phantom was filled with 105 MBq of radioactivity from the same batch. The brain phantom skull compartment was filled with a K_2HPO_4 solution supplied with the phantom, with a concentration of 100 g of salts in 67 g of water. A γ-counter (1480 Wizard 3"; Perkin Elmer) was used to determine the absolute activity concentration in the brain phantom at the PET/MR scan start time. Finally, the attenuation coefficient (μ-value) of the phantom skull was measured from the acquired CT images.

MR-Based and CT-Based Attenuation Correction for Phantom and Patients

Three μ-maps were used to evaluate the effect of MRAC on the performance of scatter correction in both the phantom and the patient

TABLE 1
Calculated Scatter Fractions in Percentages for Each Subject from Equation 1

μ-map	Scatter algorithm	Subject 1	Subject 2	Subject 3	Subject 4	Subject 5	Subject 6	Subject 7	Mean ± SD
CTAC	TF-SSS	23.54	22.83	23.59	22.41	22.43	24.61	23.82	23.32 ± 0.75
	MC-SSS	19.33	20.72	20.37	20.99	20.52	20.48	20.39	20.40 ± 0.48
MRAC$_{3class}$	TF-SSS	23.64	22.73	23.84	22.11	22.48	24.10	23.98	23.27 ± 0.75
	MC-SSS	18.85	20.01	20.25	21.52	20.11	20.47	20.54	20.25 ± 0.74
MRAC$_{2class}$	TF-SSS	23.58	22.45	23.59	21.59	22.30	24.05	23.53	23.01 ± 0.83
	MC-SSS	17.77	18.80	18.81	20.18	18.70	19.04	19.29	18.94 ± 0.67

TABLE 2
Measured Activity Values (kBq/mL) from Whole-Brain VOI with %RC Calculated by Equation 2

μ-map	Scatter algorithm	Mean (kBq/mL)	SD (kBq/mL)	Maximum (kBq/mL)	RC (%)
CTAC	TF-SSS	20.24	11.47	56.06	38.58
	MC-SSS	20.17	11.48	56.08	38.43
	Difference (%)	−0.35	0.09	0.04	
MRAC$_{3class}$	TF-SSS	18.07	10.43	51.16	34.43
	MC-SSS	18.00	10.42	51.07	34.30
	Difference (%)	−0.39	−0.10	−0.18	
MRAC$_{2class}$	TF-SSS	17.33	10.01	48.13	33.03
	MC-SSS	17.44	10.02	48.26	33.23
	Difference (%)	0.63	0.10	0.27	

study. For MRAC, a 3-class μ-map (MRAC$_{3class}$) and a 2-class μ-map (MRAC$_{2class}$) were used. The MRAC$_{3class}$ consisted of soft tissue, air, and bone, whereas MRAC$_{2class}$ included only soft tissue and air. CTAC was used as the reference μ-map. The μ-values for the MR-based μ-maps in the patient study were assigned as follows: 0.0 cm^{-1} (air), 0.096 cm^{-1} (soft tissue), and 0.151 cm^{-1} (bone) (13).

MRAC$_{3class}$ and MRAC$_{2class}$ for patients were created using a method described previously (14). MRAC$_{3class}$ was created similarly to that presented in Teuho et al. (14) whereas MRAC$_{2class}$ was created by replacing the skull μ-values with soft tissue, ignoring the patient skull. For CTAC, the head of each subject was carefully segmented out by semiautomatic regional contouring tools in Carimas 2.8 (Turku PET Centre). Thereafter, the CT Hounsfield unit values were converted to μ-values by a bilinear transformation (15).

For the phantom, MR-based μ-maps were created using MATLAB2011b (The MathWorks Inc.) and in-house software. MRAC$_{2class}$ was created by assigning a μ-value of soft tissue for the entire phantom volume segmented from CTAC. In MRAC$_{3class}$, bone was added by segmentation of the phantom skull from the CTAC and assignment of a discrete μ-value of bone to the region of the skull. The bone was assigned a μ-value of 0.128 cm^{-1}, as measured from the CT scan. CT-based μ-maps were created by segmenting out the phantom from the CTAC and by conversion of Hounsfield unit values to μ-values (15).

Finally, μ-maps were registered to non–attenuation-corrected PET images for best possible registration before image reconstruction. All images were smoothed to a PET resolution of 5 mm as in Schramm et al. (16). Example μ-maps of the phantom and 1 subject are presented in (Fig. 1).

PET Image Reconstruction and Scatter Correction

PET images were reconstructed using TF-SSS and MC-SSS. For both scatter-correction methods, 3 μ-maps were used: CTAC,

MRAC$_{3class}$, and MRAC$_{2class}$. All reconstruction parameters were fixed between TF-SSS and MC-SSS reconstructions. Reconstructions were performed using a line-of-response row action maximum-likelihood algorithm with 3 iterations and 33 subsets, a matrix size of 128 × 128 × 90, and a voxel size of 2 mm. Because of technical limitations in the reconstruction system, neither time-of-flight (TOF) nor resolution modeling was applied.

All reconstructions included the necessary corrections for image quantification: randoms, scatter, dead-time, decay, and detector normalization. Reconstructions of the clinical subjects included the head coil template and the patient table, inserted automatically by reconstruction software. The phantom image reconstructions included only the patient table because no head coil was present.

SSS and MC-SSS Sinogram Analysis

Sinograms from TF-SSS and MC-SSS were extracted from the PET reconstruction system. The randoms-corrected emission, transmission, and the final scatter sinogram from TF-SSS and MC-SSS were extracted. Sinogram radial profiles were then inspected. The profiles were averaged over all tilt angles (n = 7) and drawn over central axial bin and φ-angles.

For each method, the total scatter fraction (SF$_{total}$) from the measured sinogram data for the phantom and subjects was calculated as:

$$SF_{total} = \sum_{i=0}^{n} Events_{scatter} \Big/ \sum_{i=0}^{n} \left(Events_{prompt} - Events_{delay} \right), \quad \text{Eq. 1}$$

where (Events$_{scatter}$) is the scatter sinogram, (Events$_{prompt}$) the prompt sonogram, and (Events$_{delay}$) the delay sinogram.

Quantitative Evaluation of Phantom PET Images

Quantitative assessment of absolute activity recovery in addition to regional volume-of-interest (VOI) assessment were performed for the phantom PET images. Absolute activity recovery

TABLE 3
Calculated %RC (Eq. 2) of Regional VOI in Phantom for CTAC-Reconstructed PET

Scatter algorithm	Medial frontal cortex	Lateral frontal cortex	Orbitofrontal cortex	Temporal cortex	Cerebellum	Centrum semiovale	Basal ganglia	Cingulate cortex	Mean	SD
TF-SSS	65.50	64.92	50.34	57.49	68.23	9.62	59.49	66.77	55.29	18.13
MC-SSS	65.28	64.77	50.07	57.32	68.16	9.44	59.16	66.53	55.09	18.13

TABLE 4
Calculated Relative Difference (%Δ; Eq. 3) of Regional VOI in Brain Phantom Between TF-SSS and MC-SSS for Each μ-Map

μ-map	Medial frontal cortex	Lateral frontal cortex	Orbitofrontal cortex	Temporal cortex	Cerebellum	Centrum semiovale	Basal ganglia	Cingulate cortex	Mean	SD
CTAC	−0.34	−0.23	−0.53	−0.29	−0.11	−1.77	−0.56	−0.36	−0.52	0.49
MRAC$_{3class}$	0.27	0.20	0.09	0.33	0.38	1.46	0.34	0.34	0.42	0.40
MRAC$_{2class}$	0.45	0.33	0.29	0.49	0.53	2.51	0.61	0.55	0.72	0.68

was measured with a single VOI covering the gray matter volume and with 8 anatomic VOIs from CTAC-reconstructed PET images. Thereafter, the radioactivity from phantom PET images ($Activity_{measured}$) was measured, and the recovery coefficient (%RC) against the value measured from the γ-counter ($Activity_{calibrator}$) was calculated:

$$\%RC = Actvity_{measured}/Activity_{calibrator} \times 100. \qquad \text{Eq. 2}$$

The phantom VOI analysis was performed similarly to our previous study (17). In the analysis, the phantom PET images were coregistered and resliced to a reference volume using rigid registration on SPM8 (Wellcome Trust Centre for Neuroimaging). The reference volume size was $140 \times 140 \times 140$ pixels with a 1.22-mm isotropic resolution. Thereafter, a 5-mm gaussian postprocessing filter was applied to negate image noise. An anatomic 3-dimensional VOI set created previously (17) was used to measure radioactivity concentration in 1 deep brain and 7 cortical regions.

The mean relative difference (%Δ) between TF-SSS and MC-SSS from Equation 3 was calculated for each VOI and μ-map as follows:

$$\%\Delta = (PET_{MC\text{-}SSS} - PET_{TF\text{-}SSS})/PET_{TF\text{-}SSS}, \qquad \text{Eq. 3}$$

where $PET_{MC\text{-}SSS}$ denotes the activity measured from MC-SSS, and $PET_{TF\text{-}SSS}$ denotes the activity measured from TF-SSS.

Quantitative PET Image Evaluation of Clinical Subjects

PET images were evaluated quantitatively by VOI assessment of regional radioactivity and by ratio image analysis for visualizing regional differences. The quantitative analysis was performed using MATLAB2011b and SPM8.

VOI analysis was performed automatically, with an anatomic atlas from automated anatomic labeling software (18), using 35 cortical VOIs (Supplemental Table 1; supplemental materials are available at http://jnm.snmjournals. org) in the brain. Individualization of the atlas was based on the spatial mapping from the Montreal Neurologic Institute space to individual space using Unified Segmentation in SPM8. The atlas image was masked in the individual space using summed tissue probability maps from Unified Segmentation from gray matter, white matter, and cerebrospinal fluid with a lower threshold of 0.5.

The relative difference between TF-SSS– and MC-SSS–reconstructed PET images was assessed. The mean relative differences (%Δ) between TF-SSS and MC-SSS, with regional SDs, were calculated for each VOI and for each μ-map used in PET reconstruction from Equation 3. Linear regression analysis of MC-SSS– versus TF-SSS–reconstructed PET activity values was performed for 35 VOIs in both left and right hemispheres over 7 patients, totaling 490 points.

Additionally, pixel-by-pixel ratio images were derived by Equation 3, from which mean ratio images across all subjects were calculated for both algorithms and all μ-maps. Finally, mean PET images across all subjects were calculated using SPM8.
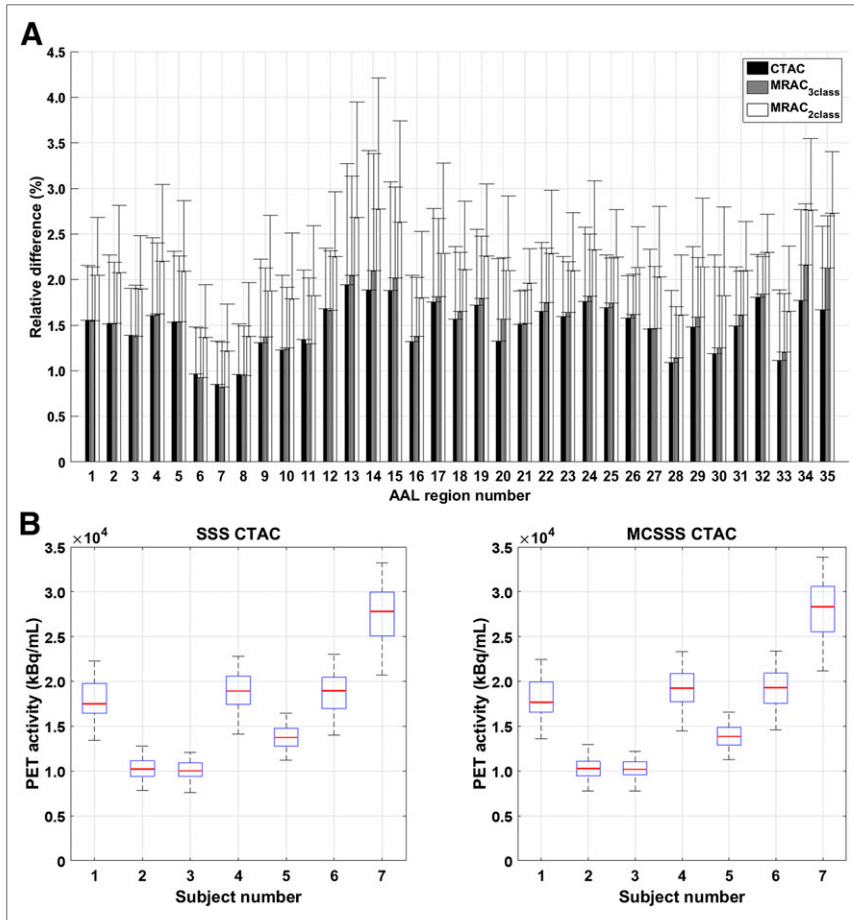

FIGURE 4. VOI analysis results of subjects between TF-SSS and MC-SSS using different μ-maps. Regional differences between TF-SSS and MC-SSS remain same regardless of μ-map used (A) and remain small subjectwise as well (B). MC-SSS results in higher reconstructed activity in A and B by 2%. Largest differences exist with MRAC$_{2class}$. Anatomic regions are listed in Supplemental Table 1.
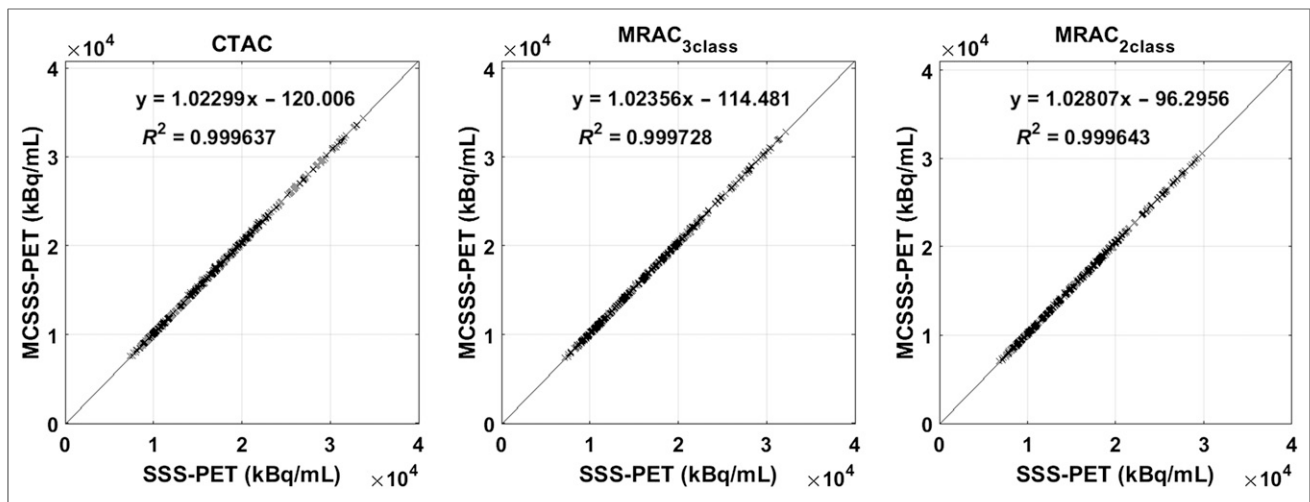
FIGURE 5. Linear regression plots from clinical subjects. TF-SSS– and MC-SSS–reconstructed PET shows excellent correlation ($R^2 > 0.99$), regardless of μ-map used.

RESULTS

Sinogram profiles from the phantom and the clinical subjects are presented in Figures 2 and 3. Additional profiles are presented in Supplemental Figures 1 and 2. A minor difference can be seen when MC-SSS is used, where CTAC has the highest and MRAC$_{2class}$ has the lowest scatter profile. There is virtually no difference in the scatter sinogram profiles with TF-SSS.

SF_{total} from Equation 1 in the phantom study for TF-SSS was 19.25% with CTAC, 19.24% with MRAC$_{3class}$, and 19.23% with MRAC$_{2class}$. SF_{total} for MC-SSS was 19.95% with CTAC, 18.35% with MRAC$_{3class}$, and 17.84% with MRAC$_{2class}$. SF_{total} from Equation 1 for individual subjects with TF-SSS or MC-SSS is presented in Table 1: only minor differences were detected with the TF-SSS algorithm.

Table 2 shows the results from the absolute activity measurement of the phantom with a whole-brain VOI, and Table 3 shows the calculated %RC in individual VOIs when CTAC was used. The %RC was calculated using a value of 45.87 kBq/mL for true activity.

Table 4 shows the results from the individual VOI analysis of the phantom study between TF-SSS– and MC-SSS–reconstructed PET for each μ-map.

The VOI analysis results of the clinical subjects are presented in Figure 4. Additional analysis is presented in Supplemental Figure 3. The mean difference between TF-SSS– and MC-SSS–reconstructed PET is smaller than 2.1% whereas the maximum difference is 4.2%.

Figure 5 shows linear regression analysis results between TF-SSS– and MC-SSS–reconstructed PET. Figure 6 presents mean PET ratio images of TF-SSS– versus MC-SSS–reconstructed PET over all subjects with each μ-map.

Finally, Figure 7 shows mean PET images over all subjects, presenting a visual comparison of TF-SSS– and MC-SSS–reconstructed PET with different μ-maps.

DISCUSSION

An evaluation of 2 scatter-correction techniques with different μ-maps for MRAC in ^{18}F-FDG PET/MR brain imaging was performed. Investigation of scatter sinograms, scatter fractions, regional quantification, and cross-correlation of reconstructed activity was performed. Two scatter-correction techniques were compared with a brain phantom and clinical subjects using 3 μ-maps in a clinical PET/MR system, for the first time to our knowledge.

Differences between TF-SSS and MC-SSS were minimal in the sinogram profiles (Figs. 2 and 3) and scatter fractions in the phantom and patient study, regardless of the μ-map used in PET reconstruction. SF_{total} remained mostly unchanged with TF-SSS whereas MC-SSS showed the lowest SF_{total} when MRAC$_{2class}$ was used both in the phantom and in the patient study. This difference in SF_{total} was 2% in the phantom study and 4% in the patient study.

Quantitatively, the absolute activity recovery and VOI analysis of the phantom showed minor differences between TF-SSS and MC-SSS regardless of the μ-map (Tables 2–4). Differences in whole-brain activity and %RC were minimal (Table 2). In VOI analysis, TF-SSS showed a slightly higher %RC than MC-SSS
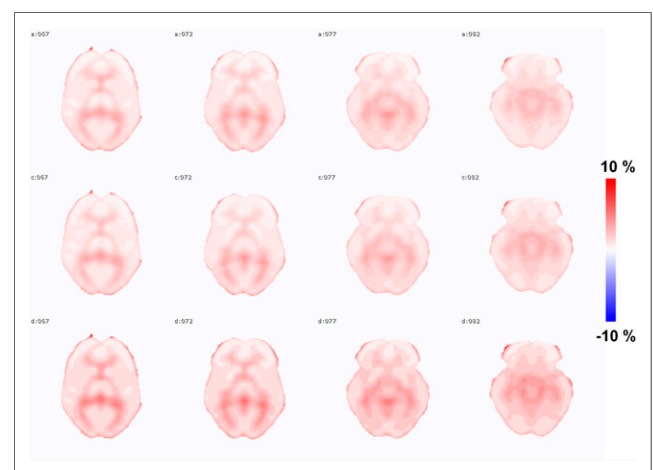

FIGURE 6. Mean ratio images calculated by Equation 3 over all subjects, pixel-by-pixel comparison of TF-SSS vs. MC-SSS. First row shows CTAC-reconstructed PET and second and third rows show MRAC$_{3class}$- and MRAC$_{2class}$-reconstructed PET, respectively. Small positive bias (<5%) in MC-SSS–reconstructed PET can be detected, which is more pronounced with MRAC$_{2class}$.
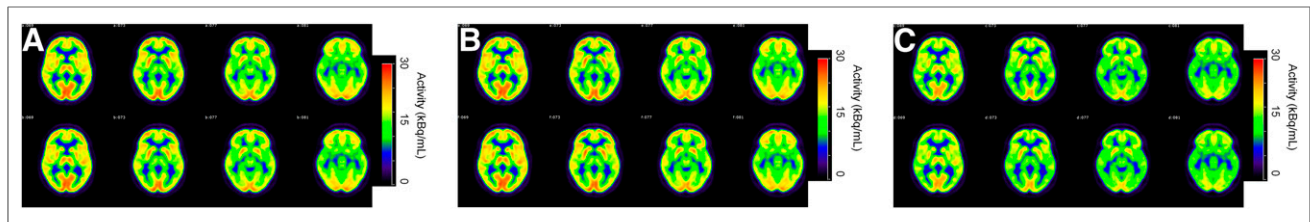
FIGURE 7. Mean PET images calculated over all subjects. (A) CTAC-reconstructed PET. (B and C) MRAC$_{3class}$- and MRAC$_{2class}$-reconstructed PET, respectively. Upper row of each subfigure denotes MC-SSS–reconstructed PET. No difference can be detected visually between TF-SSS– and MC-SSS–reconstructed PET images.

(Table 3). The mean difference between TF-SSS and MC-SSS in the phantom was 2.51% at maximum, in 1 background region with MRAC$_{2class}$ (Table 4). Thus, the quantitative performance of MC-SSS was comparable but not superior to TF-SSS (Tables 2 and 3).

Similarly, minor differences between TF-SSS and MC-SSS were detected in the patient VOI analysis, regardless of the μ-map. The difference was 2% on average and 4% at maximum (Fig. 4). The largest differences existed with MRAC$_{2class}$. Excellent correlation ($R^2 > 0.99$) was found between TF-SSS– and MC-SSS–reconstructed PET regardless of the μ-map (Fig. 5).

In MC-SSS, a positive bias was detected, which was highest with the μ-map that ignores bone (Figs. 4 and 6). In terms of final scatter fractions (4% difference) and quantitative analysis (2% mean difference), this bias can be considered to be clinically insignificant. These differences could not also be detected visually (Fig. 6). Ye et al. compared TF-SSS and MC-SSS visually with phantom and patient data in the body, concluding that both algorithms have similar visual appearance in the absence of scatter-correction artifacts (*4*).

Therefore, our study implies that scatter algorithm performance is not affected significantly by imperfections in MRAC, especially with the TF-SSS algorithm. The performance of both algorithms remained virtually unchanged regardless of the μ-map used in the PET image reconstruction. Similarly to our study, Bourgos et al. concluded that the difference between an ideal scatter estimate with CTAC and nonideal with MRAC was less than 1% with SSS algorithm in a simulation study (*2*).

Thus, the SSS algorithm remains a reliable method for scatter correction for ^{18}F-FDG brain imaging. We could not detect a specific advantage in preferring MC-SSS over TF-SSS for clinical non-TOF ^{18}F-FDG brain imaging. There are specific conditions in which another scatter-correction technique might be preferred over TF-SSS. These include head motion between emission and transmission (MRAC) (*6*); large signal voids in MRAC due to implants; and a high-activity radiotracer, for example, ^{15}O (*19*).

A limitation of our study is that only vendor-specific implementations of TF-SSS and MC-SSS were studied. Additionally, scatter algorithm performance should be investigated using TOF or radiotracers with more complex uptake than ^{18}F-FDG. Such studies are highly encouraged because scatter estimation is expected to be more challenging for tracers with specific uptake (e.g., ^{11}C-raclopride). Finally, the effect of scatter and attenuation correction in PET/MR on kinetic parameters as in the study by Mansor et al. (*7*) would be of interest.

CONCLUSION

The effect of MRAC on the performance of scatter-correction algorithms was minimal in non-TOF ^{18}F-FDG brain PET/MRI. The SSS algorithm offered consistent quantitative performance regardless of the accuracy of the MR-based μ-map. The performance of the MC-SSS algorithm was comparable but not superior to TF-SSS, warranting further investigations of algorithm optimization and performance with different radiotracers and TOF imaging.

REFERENCES

1. Watson CC. New, faster, image-based scatter correction for 3D PET. *IEEE Trans Nucl Sci.* 2000;47:1587–1594.
2. Burgos N, Thielemans K, Cardoso MJ, et al. Effect of scatter correction when comparing attenuation maps: application to brain PET/MR [abstract]. *IEEE Nucl Sci Symp Conf Rec.* 2014:1–5.
3. Mehranian A, Arabi H, Zaidi H. Vision 20/20: magnetic resonance imaging-guided attenuation correction in PET/MRI: challenges, solutions, and opportunities. *Med Phys.* 2016;43:1130–1155.
4. Ye J, Song X, Hu Z. Scatter correction with combined single-scatter simulation and Monte Carlo simulation for 3D PET [abstract]. *IEEE Nucl Sci Symp Conf Rec.* 2014:1–3.
5. Accorsi R, Adam L-E, Werner ME, Karp JS. Optimization of a fully 3D single scatter simulation algorithm for 3D PET. *Phys Med Biol.* 2004;49:2577–2598.
6. Anton-Rodriguez JM, Sibomana M, Walker MD, et al. Investigation of motion induced errors in scatter correction for the HRRT brain scanner [abstract]. *IEEE Nucl Sci Symp Conf Rec.* 2010:2935–2940.
7. Mansor S, Boellaard R, Huisman MC, et al. Impact of new scatter correction strategies on high-resolution research tomograph brain PET studies. *Mol Imaging Biol.* 2016;18:627–635.

8. Wang W, Hu Z, Gualtieri EE, et al. Systematic and distributed time-of-flight list mode PET reconstruction. *IEEE Nucl Sci Symp Conf Rec.* 2006:1715–1722.

9. Teuho J, Johansson J, Linden J, Saunavaara V, Teräs M. Comparison of single-scatter simulation and Monte Carlo single-scatter simulation on Philips Ingenuity TF PET/MR. *IEEE Nucl Sci Symp Conf Rec.* 2014:1–3.

10. Zaidi H, Ojha N, Morich M, et al. Design and performance evaluation of a whole-body Ingenuity TF PET–MRI system. *Phys Med Biol.* 2011;56:3091–3106.

11. Bettinardi V, Presotto L, Rapisarda E, Picchio M, Gianolli L, Gilardi MC. Physical performance of the new hybrid PET/CT Discovery-690. *Med Phys.* 2011;38:5394–5411.

12. Iida H, Hori Y, Ishida K, et al. Three-dimensional brain phantom containing bone and grey matter structures with a realistic head contour. *Ann Nucl Med.* 2013;27:25–36.

13. Catana C, van der Kouwe A, Benner T, et al. Toward implementing an MRI-based PET attenuation-correction method for neurologic studies on the MR-PET brain prototype. *J Nucl Med.* 2010;51:1431–1438.

14. Teuho J, Linden J, Johansson J, Tuisku J, Tuokkola T, Teräs M. Tissue probability-based attenuation correction for brain PET/MR by using SPM8. *IEEE Trans Nucl Sci.* 2016;63:2452–2463.

15. Burger C, Goerres G, Schoenes S, Buck A, Lonn AHR, Von Schulthess GK. PET attenuation coefficients from CT images: experimental evaluation of the transformation of CT into PET 511-keV attenuation coefficients. *Eur J Nucl Med Mol Imaging.* 2002;29:922–927.

16. Schramm G, Langner J, Hofheinz F, et al. Quantitative accuracy of attenuation correction in the Philips Ingenuity TF whole-body PET/MR system: a direct comparison with transmission-based attenuation correction. *MAGMA.* 2013;26:115–126.

17. Teuho J, Johansson J, Linden J, et al. Effect of attenuation correction on regional quantification between PET/MR and PET/CT: a multicenter study using a 3-dimensional brain phantom. *J Nucl Med.* 2016;57:818–824.

18. Tzourio-Mazoyer N, Landeau B, Papathanassiou D, et al. Automated anatomical labeling of activations in SPM using a macroscopic anatomical parcellation of the MNI MRI single-subject brain. *Neuroimage.* 2002;15:273–289.

19. Hori Y, Hirano Y, Koshino K, et al. Validity of using a 3-dimensional PET scanner during inhalation of ^{15}O-labeled oxygen for quantitative assessment of regional metabolic rate of oxygen in man. *Phys Med Biol.* 2014;59:5593–5609.